Revisiting Mg solubility in CuO nanorods: limit probed by neutron diffraction and effect on the particle toxicity towards bacteria in water

Batiste Clavier, Antonii Zhadan, Téo Baptiste, Fabien Boucher, Amandine Guiet, Florence Porcher, Vlasta Brezová, Christine Roques, Gwenaël Corbel

Revisiting Mg solubility in CuO nanorods: limit probed by neutron diffraction and effect on the particle toxicity towards bacteria in water

Batiste Clavier [1], Antonii Zhadan [1], Téo Baptiste [1], Fabien Boucher [2], Amandine Guiet [1], Florence Porcher [3], Vlasta Brezová [4], Christine Roques [5,6] and Gwenaël Corbel [1] *

[1] *Institut des Molécules et Matériaux du Mans (IMMM), UMR-6283 CNRS, Le Mans Université, Avenue Olivier Messiaen, 72085 Le Mans Cedex 9, France*
[2] *Institut Universitaire de Technologie du Mans, Le Mans Université, Avenue Olivier Messiaen, 72085 Le Mans Cedex 9, France*
[3] *Laboratoire Léon Brillouin, CEA-CNRS, 91191 Gif-sur-Yvette Cedex, France*
[4] *Institute of Physical Chemistry and Chemical Physics, Faculty of Chemical and Food Technology, Slovak University of Technology in Bratislava, Radlinského 9, SK-812 37 Bratislava, Slovakia*
[5] *Laboratoire de Génie Chimique, UMR-5503 CNRS, Faculté de Pharmacie, Université Paul Sabatier - Toulouse III, 35, chemin des maraîchers, 31062 Toulouse Cedex 4, France*
[6] *Centre Hospitalier Universitaire (CHU) de Toulouse, Institut Fédératif de Biologie (IFB), Laboratoire de Bactériologie et Hygiène, 330 Avenue de Grande Bretagne, 31059 Toulouse Cedex 9, France*
* *E-mail: gwenael.corbel@univ-lemans.fr ; Fax: +33 (0)2 43 83 35 06 ; Tel: +33 (0)2 43 83 26 48 ; ORCID : 0000-0003-2605-7702*

Abstract

Both nanometer-sized CuO and MgO particles exhibit bactericidal activities against *Staphylococcus aureus* and *Escherichia coli*, two bacteria causing healthcare-associated infections. The solid solution $Cu_{1-x}Mg_xO$ is potentially interesting for biomedical applications as one of the compositions could have a much higher bactericidal activity than the parent CuO and MgO oxides considered separately. But, to date, no Vegard's law proves the real existence of such a solid solution. This study was aimed at shedding light on the solubility of Mg^{2+} ions in CuO nanoparticles and its impact on the free oxygen radicals they produce, the quantity of which determines their bactericidal performance. The solid solution $Cu_{1-x}Mg_xO$ does exist and particles were synthesized as nanorods of 50–60 nm length by thermally decomposing at 400 °C the single source precursors $Cu_{1-x}Mg_x(OH)_2$. Vegard's laws exist only in the compositional range $0 \leq x \leq 0.1$, due to the low capacity of the distorted NaCl-type structure to accommodate regular coordination [MgO_6] octahedra. Only neutron diffraction allowed the detection of the small amount of MgO nanoparticles present as impurity in a 10 g sample beyond the solubility limit of x = 0.1. In this series, CuO nanorods remain the most active against *E. coli* and *S. aureus* with reduction in viability of 99.998% and 98.7% after 180 min in water, respectively. Our synthesis route has significantly increased the activity of pure CuO nanoparticles beyond the values reported so far, especially against *E. coli*. The bactericidal performances of CuO and the magnesium-substituted counterparts (*i.e.* $Cu_{1-x}Mg_xO$) are not linked to cupric ions they release in water since their mass concentrations after 180 min are much lower than minimal concentrations inhibiting the growth of *E. coli* and *S. aureus*. These CuO nanorods kill bacteria in water because they produce a large quantity of free oxygen radicals in the presence of H_2O_2 only, the majority of which are highly toxic $HO^{\bullet}$ radicals. Mg^{2+} ions have a detrimental effect on this production, thus explaining the lowest bactericidal performance of $Cu_{1-x}Mg_xO$ nanorods. Definitive knowledge of the toxicity of $Cu_{1-x}Mg_xO$ nanoparticles towards bacteria in water is now available.

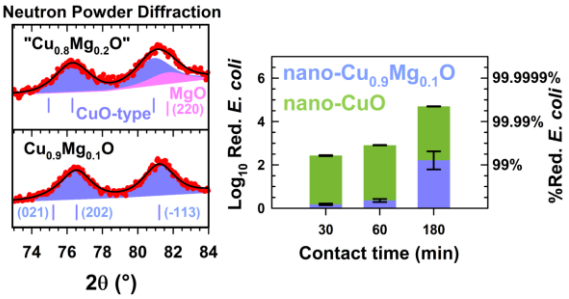

Electronic supplementary information (ESI) available: 1- Crystallographic data of $Cu_{1-x}Mg_xO$ samples from X-ray powder diffraction. 2- Le Bail fits of the neutron powder diffraction patterns of CuO (x = 0), $Cu_{0.9}Mg_{0.1}O$ (x = 0.1) and $Cu_{0.8}Mg_{0.2}O$ (x = 0.2) samples. 3- EPR spectra of the aerated water suspensions of CuO and $Cu_{0.9}Mg_{0.1}O$ (x = 0.1) nanorods in the presence of DMPO spin trapping agent. 4- IR transmission spectra of CuO (x = 0) and $Cu_{0.9}Mg_{0.1}O$ (x = 0.1) nanorods.

1-Introduction

Bacterial pathogens causing healthcare-associated infections (HAIs) pose ongoing and increasing challenges to hospitals, both in the clinical treatment of patients and in the prevention of their transmission. In 2019, a report of the agency "France Public Health"[1] pointed out that four pathogens are responsible for half of the number of HAIs in France: the two Gram-

positive bacteria *Staphylococcus aureus* (*S. aureus*, ≈13.8%) and *Enterococcus faecalis* (*E. faecalis*, ≈6.5%) together with two Gram-negative bacteria *Escherichia coli* (*E. coli*, ≈23.6%) and *Pseudomonas aeruginosa* (*P. aeruginosa*, ≈6.3%).

Several studies were devoted to the evaluation of the bacteriostatic activity of raw CuO particles towards these pathogens. Typically, evaluations by the diffusion method are carried out in a mixture of nutrient and physiological buffer media. For instance, Thakur *et al.*[2] did not measure any bacteriostatic activity against both *E. coli* and *S. aureus* within the first 24 h in contact with a suspension of CuO nanoparticles at a high concentration of 10 mg mL^{-1} in a saline Mueller–Hinton Broth (MHB) medium. In contrast, Azam *et al.*[3] estimated by following the standards of the CLSI (Clinical and Laboratory Standards Institute) that minimal concentrations of 30 and 32 μg mL^{-1} in 20 nm-sized CuO particles completely inhibit the growth of *E. coli* and *S. aureus* after 24 h in pure MHB medium, respectively. Applerot *et al.*[4] have shown that nanometer-sized particles of CuO can strongly adhere to the bacterial cell membrane. These CuO nanoparticles at a concentration of 0.1 mg mL^{-1} in saline solution mainly produce exogenous superoxide radicals $O_2^{\bullet-}/HO_2^{\bullet}$ causing the death of 99.9% of *E. coli* (3 Log_{10}) and 97% of *S. aureus* (1.5 Log_{10}) after 3 h of treatment. If discrepancies in the above results can partly be attributed to the size and the degree of agglomeration of nanoparticles, the impact of the medium components cannot be ruled out. Indeed, dissolution of CuO is reported by Hans *et al.*[5] in phosphate-buffered saline (PBS), containing chloride and phosphate anions. Gunawan *et al.*[6] showed that free amino acids in Luria Bertani Broth (LBB) culture medium also promote the dissolution of CuO nanoparticles. However, no lysis of *E. coli* cells is observed by these authors because peptides present in the LBB medium form no toxic complexes with cupric ions thus released from CuO, which considerably reduces the amount and cytotoxic effect of free Cu^{2+} on bacteria. These findings well support those of Menkissoglu *et al.*[7] who demonstrated that the Gram-negative *P. syringae* in a culture medium rich in casitones is resistant to treatments with copper sulphate even at relatively high concentrations because more than 99% of Cu^{2+} species form no toxic complexes with those peptones. To date, there is still no definitive knowledge about the toxicity of CuO nanoparticles towards bacteria because the systems studied are too complex in composition to draw a firm conclusion on the role played by released cupric ions.

Concerning the use of CuO nanoparticles as a disinfectant, the performances reported by Applerot *et al.*[4] do not meet the European performance standards of hospital/healthcare disinfection (EN 1040) which require to kill more than 99.999% of bacteria (5 Log_{10} reduction) at low concentrations. In this context, partial substitutions of cupric ions in CuO by Mg^{2+} or Zn^{2+} have also been tested up to 15 mol% by Din *et al.*[8] and Lv *et al.*[9] Growth inhibition of these bacteria is noted only after 24 h in a 0.05 mg mL^{-1} suspension of $Cu_{0.95}Mg_{0.05}O$ or $Cu_{0.97}Zn_{0.03}O$ nanoparticles in nutrient media.[9] A significant release of cupric ions from these particles is reported by these authors in a Tris buffer solution, which is not the medium they used to determine bacteriostatic activity. No conclusion on the role played by the released cupric ions in the activity can therefore be drawn, in contrast to what these authors say.[9] Furthermore, in Din *et al.*[8] and Lv *et al.*[9] studies, no clear evidence of successful Mg and Zn substitutions is given since impurity is present for some samples (additional Bragg peaks in the range $35° \leq 2\theta \leq 45°$[8]) and no linear evolution of the unit cell parameters with the substitute content (Vegard's law[10]) is shown. While only the bactericidal activity of $Cu_{0.88}Zn_{0.12}O$[11] has been evaluated, it remains completely unknown for any Mg-substituted CuO.

In this paper, nanoparticles of Mg-substituted CuO derivatives were prepared with the aim to determine the effect of their Mg content on the toxicity towards bacteria. At first, to determine how particles of CuO (and its Mg-substituted counterparts) can interact with bacteria, sterile water is the medium of choice for simplifying the system to be studied. The minimal inhibitory concentrations (MIC) of free cupric ions for *E. coli* and *S. aureus* are 25 mg L^{-1} and 12.5 mg L^{-1}, respectively.[12] It is well known that free cupric ions can catalyse the generation of ROS from aqueous H_2O_2 through a Fenton-like redox cycling between Cu^{2+} and Cu^{+}/Cu^{3+} ions.[13,14] To have a bactericidal effect against *E. coli* and *S. aureus*, the concentration of free cupric ions must be equal to or greater than the MIC. In pure water, the concentration of cupric ions released by the dissolution of CuO is 1.84 mg L^{-1} at 25 °C[15] which is below the MIC. Theoretically, the reductions in cell viability that we will measure in water suspension of CuO nanoparticles will only result from the intrinsic toxicity of nanoparticles. Secondly, to probe the solubility of Mg in CuO nanoparticles, we combined microstructural analyses of five different compositions from X-ray diffraction data using the integral breadth method with Le Bail fits of neutron diffraction patterns collected on 10 g samples of three selected compositions. These thorough analyses definitively show that such mixed oxides $Cu_{1-x}Mg_xO$ do exist as a single phase in a defined range of compositions. Our recent study reveals that 10–20 nm-sized MgO particles completely dissolve in water over a 3 h period.[16] As the Mg substitution in CuO should thereby favour a partial dissolution of the nanoparticles in water, atomic emission spectroscopy (AES), X-ray powder diffraction (XRPD) and infrared (IR) spectroscopy are used to quantify the amount of free cupric and magnesium ions in the supernatant and to detect any trace of hydroxides formed. Against all expectations, the mass concentration of free cupric ions in the water suspension of $Cu_{0.9}Mg_{0.1}O$, although slightly higher than that for CuO, also remains below the MIC. The toxicity of pure and Mg-substituted CuO nanorods towards *E. coli* or *S. aureus* is therefore not linked to the very few free cupric ions present in water. Free oxygen radicals were in parallel tracked in the particle suspension of CuO and $Cu_{0.9}Mg_{0.1}O$ by electron paramagnetic resonance (EPR) spin trapping experiments. These results provide the key to the toxicity of CuO in water and the impact of magnesium substitution on it.

2-Materials and methods

2-1) Starting materials

The single source precursor $Cu_{1-x}Mg_x(OH)_2$ was prepared at room temperature through a co-precipitation synthesis route extensively described in ref. 17. Hydrogen peroxide (for analysis, 30%), 5,5-dimethyl-1-pyrroline *N*-oxide (DMPO) and 4-hydroxy-2,2,6,6-tetramethylpiperidine-*N*-oxyl (TEMPOL) were purchased from Sigma-Aldrich. DMPO was distilled prior to use.

2-2) Synthesis

One gram of nanometer-sized particles of mixed $Cu_{1-x}Mg_xO$ oxides were obtained by thermally decomposing ≈1.2 g of $Cu_{1-x}Mg_x(OH)_2$ for 12 h at 400 °C in air (heating rate of 3 °C min^{-1}). The decomposition temperature was determined by thermogravimetry (TG) and mass spectrometry (MS) of the evolved gas in ref. 17. Once synthesized, raw nanoparticles were stored in an argon-filled glove box with less than 1 ppm in water to avoid the formation of any hydroxide by-products prior to any analysis. For three $Cu_{1-x}Mg_xO$ compositions (x = 0, 0.1 and 0.2), the above process was performed ten times in order to get the 10 g of sample required for the neutron diffraction study.

2-3) X-Ray powder diffraction (XRPD) and neutron powder diffraction (NPD)

The phase purity of the as-prepared nanometer-sized particles was checked by recording X-ray powder diffraction (XRPD) patterns at room temperature on a PANalytical θ/θ Bragg–Brentano Empyrean diffractometer ($CuK\alpha_{1+2}$ radiations) equipped with a PIXcel^{1D} detector. The raw powders were dusted through a 63 µm sieve on a glass holder under an ambient air atmosphere (RH 60%). XRPD patterns were collected at room temperature in the [5°–135°] scattering angle range, with a 0.0131° step size, for a total acquisition time of 330 min. The data collection was performed on raw nanoparticles right out of the glove box to avoid the formation of the hydroxide by-product when exposed to an ambient air atmosphere (60% RH). The apparent size S_β and the average lattice strain $\langle\varepsilon_\beta\rangle$ of nanometer-sized particles were determined from diffraction data by the integral breadth method.[18–21] The patterns of the reference material $Na_2Ca_3Al_2F_{14}$ (NAC[22]) and the studied samples were refined by the Le Bail method[23] with the Fullprof program[24] using a modified Thompson–Cox–Hastings pseudo–Voigt profile function[25] (referred to as TCH-Z function) in which the size-broadening and microstrain-broadening effects both contribute to the Lorentzian and Gaussian components of the line widths. The "needle vector size" model of the Fullprof program was selected with the [0k0] direction parallel to the revolution axis of the needle. In a simplified approach, the size-broadening effect was assumed to contribute only to the Lorentzian component (two adjustable parameter) of the line widths, while the Gaussian component (one adjustable parameter) would only arise from microstrain. The apparent size S_β and the average lattice strain $\langle\varepsilon_\beta\rangle$, were then calculated from those two components, respectively.[26]

10 g of $Cu_{1-x}Mg_xO$ nanoparticles (x = 0, 0.1 and 0.2) were loaded in a cylindrical vanadium can (⌀ = 10 mm) for recording neutron powder diffraction (NPD) pattern data at room temperature. NPD patterns were recorded on a two axis G4.4 diffractometer at the Orphée reactor of the Laboratoire Léon Brillouin (LLB, CEA Saclay, France) with a single incident wavelength of 1.95226 Å selected by a (224) Ge curved monochromator. The intensities were measured using a bank of 70 ^{3}He detectors in the 2θ scattering angle range [4°–100°] with a 0.05° step. The line-shape was modelled by a Thompson–Cox–Hastings pseudo–Voigt function (refined parameters U, W, Y).[22] The background intensity was estimated from linear interpolation between up to 11 points manually selected in regions free of Bragg reflections of CuO-type phase (space group $C\,2/c$ (no.15)).

2-4) Morphology and size of nanoparticles

Imaging the nanometer-sized particles by TEM was performed on a JEOL JEM 2100 HR electron microscope operating at an accelerating voltage of 200 kV and equipped with a side entry ±35° double-tilt specimen holder. The sample for TEM investigation was prepared by ultrasonically dispersing the particles in absolute ethanol, depositing a drop of the resulting suspension onto a holey carbon-coated copper grid and finally drying the grid in air. N_2 adsorption measurements were performed at −196 °C on a Micromeritics TriStar II 3020 Instrument (Micromeretics, Norcross, GA). Prior to any surface area measurement, water vapor and gases adsorbed onto the grain surface were desorbed under primary vacuum by using a Micromeritics VacPrep 061 degasser. Approximately 400 mg of powder was employed in each measurement. All samples exhibit a type II adsorption isotherm typical of nonporous solids. The specific surface area was calculated using the Brunauer–Emmett–Teller (BET) model.[27]

2-5) Bactericidal activity experiments

The evaluation of the bactericidal activity of the oxide particles was carried out at 20 °C against two strains obtained from the Institute Pasteur Collection (Paris, France): *Staphylococcus aureus* CIP 4.83 and *Escherichia coli* CIP 53.126. The as-prepared oxide particles were dispersed at 20 °C in sterile distilled water to obtain a suspension with an initial concentration of 1 mg mL^{-1}. For each strain, 10 mL of each nanoparticle suspension were inoculated with 100 µL of bacterial suspension, thus leading to a final concentration of bacteria of ≈2 × 10^6 colony forming units per mL. A bacterial suspension without nanoparticles was used as a positive control. The suspensions were then maintained at 20 °C under constant stirring on a rotary platform working at 250 shakes per min. At specified times (15, 30, 60 and 180 min), 1 mL of each suspension and of the corresponding serial ten-fold dilutions were incorporated into trypticase soy agar medium poured in flat-bottomed Petri dishes and plates were incubated at 36 °C for 48 h. The viable cell number was determined by counting the number N of bacterial colonies grown (CFU), multiplied by the dilution factor and expressed as CFU mL^{-1} of the suspension under test. The

results are expressed in CFU counts N_t at a contact time t (N_0 at $t = 0$), in percent reduction in cell viability $[(N_0 - N_t) \times 100]/N_0$ as well as in $R\,\mathrm{Log}_{10}$ reduction ($R = \mathrm{Log}_{10}(N_0/N_t)$). The experiments were repeated two times for each tested strain.

2-6) Stability of nanoparticles in water

30 mg of each studied powder are immersed at room temperature in deionized water at a final concentration of 10 mg mL^{-1} without agitation. A powder fraction was taken after 960 min of immersion, then blended with acetone and diethyl ether $(C_2H_5)_2O$ to stop any hydration reaction and finally dried in air at room temperature. XRPD patterns and infrared (IR) spectra were then collected on these exposed powders. The XRPD patterns were collected with the same diffractometer in the [30°–55°] scattering angle range, with a 0.0394° step size, for a total acquisition time of 12 min. IR transmission spectra were collected with an Alpha Bruker Fourier transform infrared (FT-IR) spectrometer equipped with the "Platinum" QuickSnap™ ATR sampling module. Each spectrum was obtained after 25 scans in the 4000–400 cm^{-1} range with a spectral resolution of 4 cm^{-1}. A reference IR spectrum was collected under the same conditions without any sample and subtracted from spectra collected on specimens in order to remove the contribution of atmospheric water vapor and carbon dioxide gas. Atomic emission spectroscopy (AES) has been used for measuring the amount (down to 0.05 ppm) of magnesium and copper elements possibly released from the studied powder in deionized water. Nanoparticles are immersed in deionized water at a final concentration of 1 mg mL^{-1} without agitation for 180 min. Concentrations in magnesium and copper ions in the supernatant were determined by using a 4100 Micro Plasma-Atomic Emission (MP-AES) spectrometer from Agilent Technologies. The apparatus is equipped with a OneNeb nebulizer and a double-pass cyclonic spray chamber. The analytical cycle consisted of 15 s of sample uptake (pump speed 40 rpm), and then 15 s of stabilization before performing three replicates. Calibration solutions were prepared by dilution of the ICP multi-element standard VIII solution (100 mg L^{-1}, Merck) in the range of 0.05–10 mg L^{-1}. 5 mL of supernatant solution were manually introduced using a capillary. Integration time was set to 3 s both for magnesium and copper ions. Calibrations functions for the MP-AES measurements were linear up to 10 mg mL^{-1} for copper ions ($r^2 > 0.999$, 324.754 nm) and 5 mg mL^{-1} for magnesium ions ($r^2 > 0.995$, 285.213 nm).

2-7) EPR spin trapping experiments

The stock suspensions of CuO and $Cu_{0.9}Mg_{0.1}O$ nanoparticles (2 mg mL^{-1}) were prepared in deionised water. The spin trapping agent DMPO and hydrogen peroxide were dissolved in deionised water. The EPR spectra of nanoparticles in X-band (modulation frequency of 100 kHz) were measured using an EMX*plus* spectrometer (Bruker) with a high sensitivity probehead (Bruker) in the Wilmad® quartz (CFQ) EPR tubes (O.D. = 2 mm, L = 100 mm) at 20 °C (data not shown); the experiments with the aqueous suspensions were performed using a small quartz flat cell (WG 808-Q, Wilmad-LabGlass). The suspensions containing nanoparticles at a concentration of 2 mg mL^{-1} were mixed with DMPO and H_2O_2 stock solutions 2 min before recording the first EPR spectrum at 20 °C. In that way, the final concentration in nanoparticles within the analyzed suspension is 1 mg mL^{-1} as used in the bactericidal tests. The EPR spectra of DMPO-adducts were recorded every 5 min to follow their evolution during the first 20 min (4 consecutive recordings). Each spectrum was obtained by the accumulation of 10 scans of 30 seconds each. The experiments were repeated at least in triplicate. The *g*-values of DMPO spin-adducts were determined with an uncertainty of ±0.0001 using a nuclear magnetic resonance teslameter and integrated frequency counter. The concentration of DMPO spin-adducts was evaluated from the double-integrated EPR spectra based on the calibration curve obtained from the EPR spectra of TEMPOL solutions measured under strictly identical experimental conditions. The experimental EPR spectra were analyzed using WinEPR software (Bruker) and the simulated spectra were calculated using the EasySpin toolbox.[28] EPR spectrometer settings in the spin trapping experiments: microwave frequency, ~9.43 GHz; microwave power, 21.4 mW; center field, ~335.8 mT; sweep width, 8 mT; gain, 2.00×10^5; modulation amplitude, 0.05 mT or 0.1 mT; sweep time, 30 s; time constant, 5.12 ms; number of scans, 10.

3-Results and discussion

3-1) Phase identification of nanoparticles

Mixed $Cu_{1-x}Mg_xO$ oxides were prepared through the thermal decomposition of the single source precursors $Cu_{1-x}Mg_x(OH)_2$ at a moderate temperature of 400 °C. Prior to decomposition, we checked by EDX analysis that the precursor particles had the expected Mg/Cu atomic ratio.[17] X-ray powder diffraction (XRPD) patterns were recorded after decomposition to determine the phase purity of as-obtained powders. In Fig. 1a, the XRPD patterns of raw powders seemingly show a single CuO-type phase (tenorite) in the whole compositional range investigated $0 \leq x \leq 0.2$.

Refinements of the crystal structures of the different $Cu_{1-x}Mg_xO$ oxides were attempted from those XRPD patterns by the Rietveld method[29] of the Fullprof program[24] using the monoclinic crystal structure of tenorite CuO, as a starting structural model.[30] The profile shape of all Bragg reflections located at scattering angles higher than 60° in 2θ remain unsatisfactorily modelled by least-squares fitting of this structural model. This problem arises from the strong overlapping of Bragg peaks which are highly broadened by the shape and the nanometer size of the coherently diffracting domains in $Cu_{1-x}Mg_xO$ particles, only (Fig. 1a). All the Bragg peaks have a symmetric Voigt-type profile which makes possible a microstructural analysis from XRPD data using the Integral Breadth method,[18–21] as described in the Experimental section 2.3. Such analysis will also allow us to evaluate the effect of magnesium substitution on the monoclinic cell parameters. In the

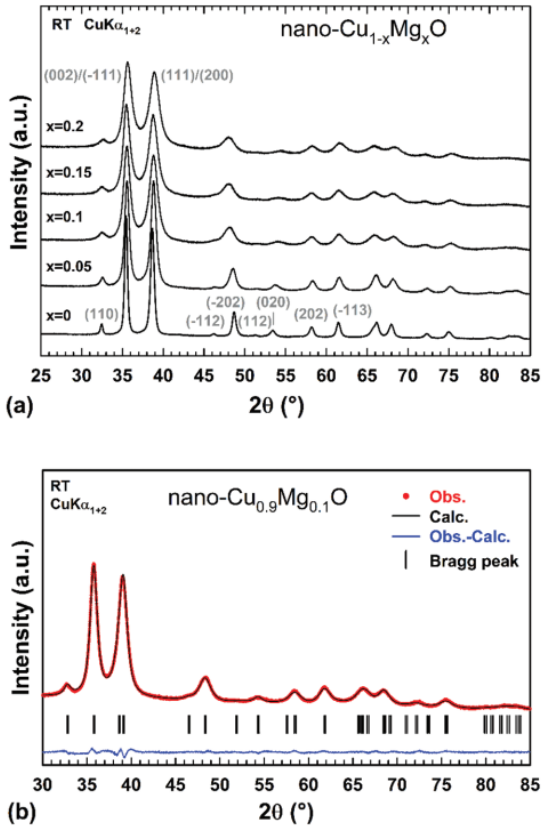

Fig. 1 (a) XRPD patterns recorded under an ambient air atmosphere (60% RH) and room temperature (RT) for nanometer-sized $Cu_{1-x}Mg_xO$ particles for different magnesium contents *x*. The (*hkl*) values of the first crystal planes are given. (b) Comparison of the observed diffraction pattern of nanometer-sized $Cu_{0.9}Mg_{0.1}O$ (x = 0.1) particles (red dots) with the pattern calculated by the integral breadth method (black line). The blue curve corresponds to the difference between observed and calculated patterns. Vertical markers give Bragg peak positions for the CuO-type phase (space group *C*2/*c* (no. 15)).

present analysis, the peak broadening is assumed to originate from both the nanometer size (the "size broadening" effect) and the lattice distortion ("microstrain broadening" effect) of coherently diffracting domains. For each $Cu_{1-x}Mg_xO$ sample, the a, b, c and β parameters of the monoclinic unit cell together with the apparent size S_β and the average lattice strain $\langle\varepsilon_\beta\rangle$ of those nanodomains were determined from the refinement of the XRPD patterns by the Le Bail method[23] of the Fullprof program.[24] As shown in Fig. 1b for $Cu_{0.9}Mg_{0.1}O$, the observed diffraction patterns of all samples can be satisfactorily fitted using the integral breadth method. The values of the a, b, c and β parameters of each $Cu_{1-x}Mg_xO$ sample are reported in Table S1 of the ESI (section S1†). The variations of the monoclinic cell parameters, S_β and $\langle\varepsilon_\beta\rangle$ are shown in Fig. 2a and c as a function of the magnesium content x in the $Cu_{1-x}Mg_xO$ nanoparticles.

As the magnesium content x increases in the compositional range $0 \le x \le 0.1$, the unit cell deforms significantly in the basal (a,c) plane by expanding along the a axis and contracting very slightly along the c axis while opening the β angle between these two axes (Fig. 2a). In addition, a contraction of the unit cell along the b axis is also noted with increasing x up to x = 0.1 (Fig. 2a). These linear evolutions of the four cell parameters in the range $0 \le x \le 0.1$, therefore, follow the usual Vegard's laws.[10] It attests the formation of a substitutional $Cu_{1-x}Mg_xO$ solid solution in this limited composition range. For each cell parameter, a departure from linearity with a kind of levelling off is observed above x = 0.1 (Fig. 2a). The solubility limit of Mg^{2+} ions in the cationic sub-lattice of CuO should be between x = 0.1 and 0.15 although no trace of MgO is detectable as secondary phase in the XRPD patterns of the x = 0.15 and 0.2 samples (Fig. 1a).

Despite several attempts, no fit of the XRPD pattern with a major CuO-type and a minor MgO phases provide convincing evidence for the biphasic nature of the x = 0.2 sample. In order to prove that Mg-solubility in CuO does not exceed x = 0.1, neutron diffraction patterns (NPD) were recorded for 10 g samples of three selected $Cu_{1-x}Mg_xO$ compositions (x = 0, 0.1 and 0.2) of the series. With this large amount of powder, we hoped to be able to detect trace amounts of MgO in the x = 0.2 sample and conversely prove its absence in the x = 0.1 one. For each sample, a refinement of the NPD pattern was carried out by the Le Bail method[23] of the Fullprof program.[24] For the x = 0 and 0.1 samples, the NPD patterns were satisfactorily modelled with a single CuO-type phase, as shown in Fig. S1 of the ESI (section S2†). On the other hand, such a fit is not satisfactory for the x = 0.2 sample, in particular on the high scattering angle side of the (−113) Bragg peak located at 2θ of around 80.9°, for which the intensity calculated above 81.5° for a single CuO-type phase remains lower than that measured. In Fig. 3b, this situation is not, however, encountered for the x = 0 and 0.1 samples, thus attesting unequivocally to their monophasic character. As the position in 2θ of this shoulder corresponds to the (220) Bragg peak of MgO, a fit of the NPD pattern was then carried out with a major CuO-type phase and MgO as secondary phase. As shown in Fig. 3a and b, a good match between observed and calculated NPD patterns is now obtained for the x = 0.2 sample. For the x = 0, 0.1 and 0.2 samples, the values of the monoclinic cell parameters obtained from NPD data are close to those deduced from the XRPD data, despite their much lower accuracy (Table S2 in section S2 of the ESI†). The NPD study confirms the evolution of the cell parameters as a function of the magnesium content x, as pointed out in Fig. 2a: the limit of the solid solution $Cu_{1-x}Mg_xO$ is x = 0.1 and not x = 0.07 as suggested by Lv *et al.*[9]

Our thorough analysis clearly shows that a simple visual inspection of the XRPD patterns in Fig. 1a, as done by Lv *et al.*[9] in their study, cannot determine up to what threshold value the substitution of copper by magnesium is really effective within the nanoparticles. Indeed, the peaks characteristic of the presence of MgO nanoparticles as an impurity cannot be detectable in the background of the XRPD patterns

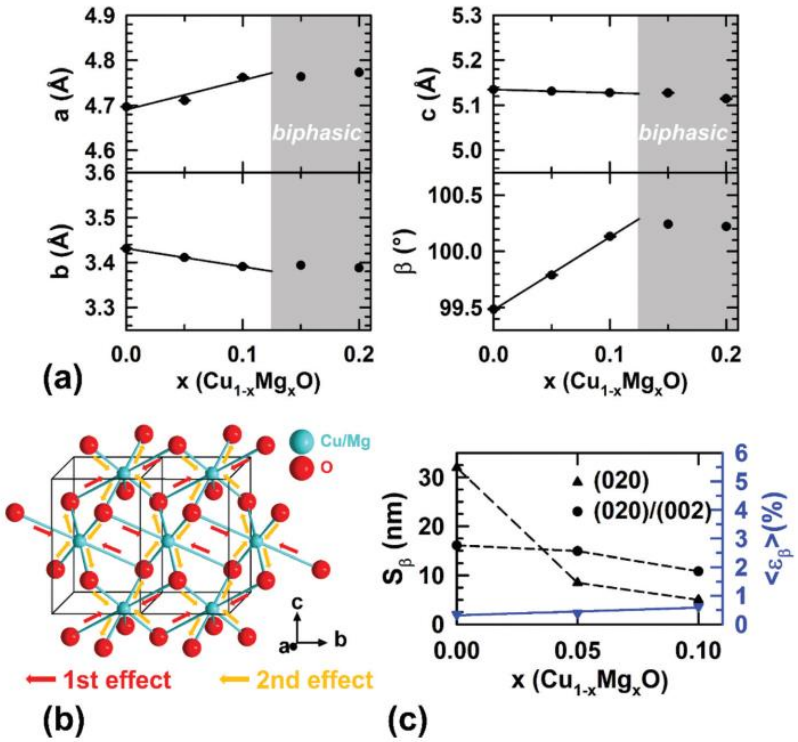

Fig. 2 (a) Monoclinic cell parameters of the $Cu_{1-x}Mg_xO$ compounds for each magnesium content x. (b) Sketch of the predictive deformation of the CuO crystal structure caused by the partial substitution of copper by magnesium. Each arrow gives the direction in which the deformation of the Cu/Mg–O bond occurs. (c) Variations of the average lattice strain $\langle\varepsilon_\beta\rangle$ and the apparent size S_β of the coherently diffracting domains along different crystallographic directions with the magnesium content x in nanometer-sized $Cu_{1-x}Mg_xO$ particles.

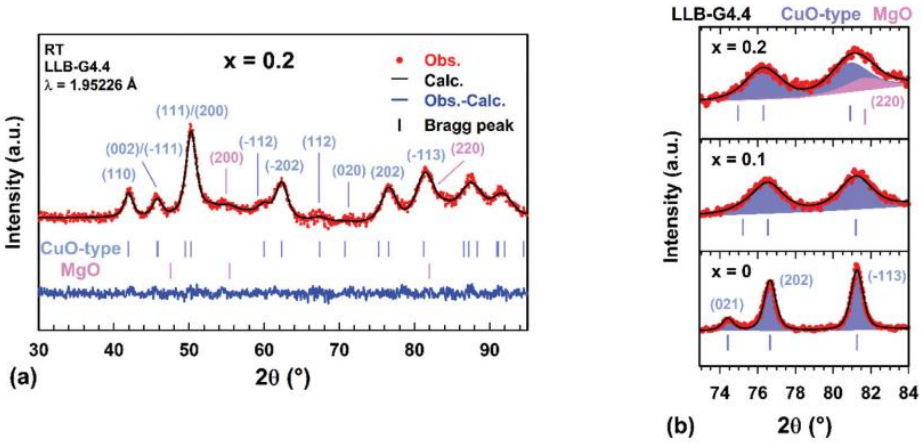

Fig. 3 (a) Comparison of the observed NPD patterns (red dots) of the "$Cu_{0.8}Mg_{0.2}O$" (x = 0.2) raw powder sample with the pattern calculated by the Le Bail method (black line) considering that MgO is present as an impurity in addition to a major CuO-type phase. The blue curve corresponds to the difference between observed and calculated patterns. Vertical markers give Bragg peak positions for MgO and the CuO-type phase (space groups $Fm\bar{3}m$ (no. 225) and $C2/c$ (no. 15), respectively). The (hkl) values of the different crystal planes are also given. (b) Evidence for the presence of MgO as an impurity in the 2θ scattering angle range [73–84°] of the observed NPD pattern of the "$Cu_{0.8}Mg_{0.2}O$" (x = 0.2) raw powder sample.

(collected on a few hundred milligrams, at best) due to their very low intensity and large width of its Bragg peaks. The limited 2θ range and resolution of NPD patterns of the $x = 0.2$ sample does not allow the amount of MgO present to be accurately quantified by refinement using the Rietveld method.[29] In our previous study (thanks in particular to thermal analyses),[17] we found that the solubility limit of Mg^{2+} ions in $Cu(OH)_2$ is 10 mol% (*i.e.* $Cu_{0.9}Mg_{0.1}(OH)_2$). Since the same solubility limit is found for Mg^{2+} ions in CuO and $Cu(OH)_2$ (*i.e.* 10 mol%), we conclude that the Cu/Mg atomic ratio in the oxide nanoparticles is identical to what it was in the hydroxide nanoparticles used as precursors. We believe that the solubility of divalent *M* cations in CuO (*i.e.* $Cu_{1-x}M_xO$) is dependent on the difference in ionic radii $|\Delta r_i| = |r_i(Cu^{2+}) - r_i(M^{2+})|$. The solubility of Co^{2+} ions in CuO is low ($x(Co^{2+}) \leq 0.05$ [31]) because the difference in ionic radii is large ($|\Delta r_i| = 0.08$ Å [32]). When compared with Co^{2+}, the solubility of Mg^{2+} ions still reaches $x(Mg^{2+}) = 0.10$ because this time $|\Delta r_i| = 0.01$ Å [32] is very small. Continuing with this reasoning, the solubility limit of Zn^{2+} ions in CuO should be less than or equal to that of Mg^{2+} ions (*i.e.* 10 mol%) because these two substitutes have the same difference in ionic radii $|\Delta r_i|$ with Cu^{2+}. Moreover, traces of ZnO as secondary phase are detectable in the XRPD pattern collected on $Cu_{0.9}Zn_{0.1}O$ nanoparticles by Lv *et al.*[9] To our opinion, the high bactericidal performance of $Cu_{0.88}Zn_{0.12}O$ [11] may result from the synergistic bactericidal actions of nanoparticles of more lightly Zn-substituted CuO and pure ZnO, without these authors having apparently detected by diffraction the minute quantities of the latter. To clarify this point, the phase purity in a 10 g sample of "$Cu_{0.88}Zn_{0.12}O$" should be determined using neutron diffraction, as we did.

Although no satisfactory Rietveld refinement of the crystal structure could be carried out for the different $Cu_{1-x}Mg_xO$ oxides, an explanation for the evolutions of cell parameters can nevertheless be proposed. The monoclinic structure of tenorite CuO (space group *C*2/*c* (no. 15)) can be viewed as a highly distorted NaCl-type structure[30] built from edge-sharing $[CuO_6]^{10-}$ octahedra (Fig. 2b). The Mg^{2+} ion (ionic radius = 0.72 Å (CN = 6)[32]) is slightly smaller in size than the cupric cation when six-fold coordinated to oxygen (ionic radius = 0.73 Å (CN = 6)[32]). The coordination $[CuO_6]^{10-}$ octahedra are distorted with two long apical Cu–O distances (2.784(4) Å) and four short equatorial Cu–O distances (2 × 1.951(3) Å and 2 × 1.961(1) Å). Note that, these Cu–O bond lengths are much longer or slightly shorter than the sum of ionic radii $r_{Cu} + r_O =$ 2.09 Å (with $r_O = 1.36$ Å when considering this oxygen atom in an $[OCu_3]^{4+}$ environment[32]). This high [4 + 2] distortion originates from the Jahn–Teller effect of cupric ions ($3d^9$) which induces a huge elongation of the octahedral coordination along its 4-fold axis. Mg^{2+} ions cannot generate such an effect because of its electronic configuration. The $[MgO_6]^{10-}$ octahedron should thereby be quite regular with Mg–O bond lengths corresponding roughly to the sum of ionic radii $r_{Mg} + r_O = 2.08$ Å as in MgO. Because all edges of each $[CuO_6]^{10-}$ octahedron are shared with the next neighbouring polyhedra in the crystal structure of CuO, the replacement of a few elongated $[CuO_6]^{10-}$ octahedra by more regular $[MgO_6]^{10-}$ ones necessarily changes all metal–oxygen bond lengths, as shown by the arrows in Fig. 2b. Indeed, the displacements of oxygen atoms caused by the shortening of the mean apical (Mg/Cu)–O distances of the octahedra (red arrows in Fig. 2b) decrease and increase the mean equatorial (Cu/Mg)–O distances (orange arrows in Fig. 2b). Probably, all oxygen–metal–oxygen bond angles are also affected by these displacements of oxygen atoms (not highlighted in Fig. 2b). This predictive deformation of the dense network of edge-sharing $[(Cu/Mg)O_6]^{10-}$ octahedra (Fig. 2b) provides a realistic explanation for the antagonistic effects of the magnesium substitution on the cell dimensions displayed in Fig. 2a.

In Fig. 2c, a reduction in the apparent size S_β of the coherently diffracting domains by almost 75% is noted along the *b* axis as soon as the sample contains 5 mol% of magnesium while remaining unchanged in the basal (*a*,*c*) plane. The average lattice strain $\langle \varepsilon_\beta \rangle$ is high and slightly increases from 0.3 to 0.6% upon substitution (Fig. 2c). In the structure of $Cu(OH)_2$,[17] the dehydroxylation of the staircase-shaped $[Cu(OH)_2]_\infty$ layers stacked along the *b* axis allows their condensation (oxolation) in order to build the three dimensional network of edge-sharing octahedra found in the structure of CuO. High lattice distortions then appear during this oxolation at the reaction interface between just condensed and still hydroxylated layers due to the local reduction of the packing metal–metal distance. We have observed a similar behaviour during the thermal decomposition of $Mg_{1-x}Cu_x(OH)_2$ into $Mg_{1-x}Cu_xO$.[16]

Since the limit of the solid solution $Cu_{1-x}Mg_xO$ is $x = 0.1$, the next sections focus on the three single-phase samples CuO, $Cu_{0.95}Mg_{0.05}O$ and $Cu_{0.9}Mg_{0.1}O$ only. Before evaluating the bactericidal activity of these three compositions, the morphology and the size of their nanoparticles were determined by transmission electron microscopy (TEM). The following section is devoted to this investigation.

3-2) Morphology and size of nanoparticles

The TEM images of the particles of CuO, $Cu_{0.95}Mg_{0.05}O$ and $Cu_{0.9}Mg_{0.1}O$ are shown in Fig. 4. Nitrogen sorption measurements were also carried out to determine the specific surface areas (SSA) of the studied powders. The particles of CuO ($x = 0$ in Fig. 4a) consist of bulging rods of 60 nm length and 30 nm diameter on average. Due to the strong agglomeration of these nanoparticles with each other, the CuO powder exhibits a low SSA of ≈8 $m^2\ g^{-1}$ (Fig. 4a). Conversely, the $Cu_{0.9}Mg_{0.1}O$ powder ($x = 0.1$ in Fig. 4c) is composed of thin rods of 50 nm in length and 10 nm in diameter. These nanorods are weakly agglomerated to each other within the $Cu_{0.9}Mg_{0.1}O$ powder, thus leading to an SSA of ≈54 $m^2\ g^{-1}$ (Fig. 4c). A difference in SSA was previously observed between the single source $Cu_{0.9}Mg_{0.1}(OH)_2$ (81 $m^2\ g^{-1}$) and $Cu(OH)_2$ (17 $m^2\ g^{-1}$) precursors from which the oxides were derived.[17] The nanorods of $Cu_{0.95}Mg_{0.05}O$ have a length/diameter ratio intermediate between those of CuO and $Cu_{0.9}Mg_{0.1}O$ (Fig. 4b). However, the

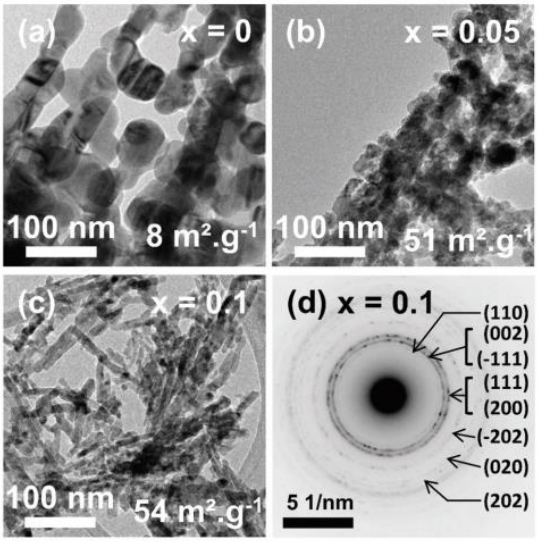

Fig. 4 (a–c) TEM micrographs of nanometer-sized $Cu_{1-x}Mg_xO$ particles for different magnesium contents x. Specific surface area determined from N_2 adsorption measurements are given. (d) SAED pattern of slightly agglomerated $Cu_{0.9}Mg_{0.1}O$ particles (x = 0.1).

powder of $Cu_{0.95}Mg_{0.05}O$ has a similar SSA to that of $Cu_{0.9}Mg_{0.1}O$ because the agglomeration degree of $Cu_{0.95}Mg_{0.05}O$ nanorods is lower than that of CuO ones.

Note that, the dimensions of $Cu_{1-x}Mg_xO$ nanorods measured from TEM micrographs are larger than the apparent size S_β of the coherently diffracting domains calculated from XRPD patterns along the different crystallographic directions (Fig. 2c). Several coherently diffracting domains with different orientations necessarily coexist within each nanorod appearing on TEM images (Fig. 4). For each oxide, the selected area electron diffraction (SAED) pattern collected on several nanorods shows eight distinct rings, as shown in Fig. 4d for the x = 0.1 sample. The presence of rings rather than individual diffraction spots results from the superimposition of the SAED patterns of the numerous nanorods analyzed at the same time. These six rings are indexed to the crystal planes of a CuO-type structure (Fig. 4d) with inter-reticular d_{hkl} distances in very good agreement with those of the first six most intense Bragg diffraction peaks in the XRPD patterns displayed in Fig. 1a. It thus confirms the high crystallinity of the nanorods of $Cu_{1-x}Mg_xO$ we synthesized.

3-3) Bactericidal activity

The bactericidal activity of $Cu_{1-x}Mg_xO$ nanorods against *E. coli* CIP 53126 and *S. aureus* CIP 4.83 was evaluated as a function of time (15, 30, 60 and 180 min) in sterile distilled water with a concentration in particles of 1 mg mL^{-1}. This concentration is identical to the one used by Malka *et al.*[11] for evaluating the bactericidal activity of $Cu_{0.88}Zn_{0.12}O$, thus allowing comparisons. For both *E. coli* and *S. aureus*, the number N_t of CFU at different times in contact with CuO, $Cu_{0.95}Mg_{0.05}O$ and $Cu_{0.9}Mg_{0.1}O$ nanorods are displayed in Table 1. In this table, the results show that the reductions in the viability of *E. coli* with the nanorods of CuO are between 2 and 3 Log_{10} for contact times of less than 60 min before increasing up to 4.7 Log_{10} after 180 min. The nanorods of CuO are active against *S. aureus* only after 180 min with a reduction in the viability of about 2 Log_{10}. The partial substitution of cupric ions by Mg^{2+} in the structure of CuO has a detrimental effect on its bactericidal kinetics against *E. coli* since the reductions remain less than 0.5 Log_{10} after 60 min without going beyond 2.5 Log_{10} after 180 min for the richest magnesium x = 0.1 sample. This result is surprising because the SSA of CuO nanorods is smaller than that of their Mg-substituted counterparts (Fig. 4). While nanorods of CuO were not active against *S. aureus* for contact times less than 60 min, more than 60% (≈0.5–0.6 Log_{10}) of these bacteria are killed by nanorods of $Cu_{0.95}Mg_{0.05}O$ and $Cu_{0.9}Mg_{0.1}O$ in this time period. The beneficial effect of magnesium is nevertheless limited in time as the reductions in cell viability after 180 min for $Cu_{0.9}Mg_{0.1}O$ do not exceed that for CuO. In order to elucidate this point,

Table 1 Bactericidal activity of $Cu_{1-x}Mg_xO$ nanorods (1 mg mL^{-1}) against *E. coli* CIP 53126 and *S. aureus* CIP 4.83 as a function of the magnesium content x (average value ± standard deviation over 2 independent assays)

		E. coli			*S. aureus*		
Magnesium content x	Contact time (min)	$Log_{10} N_0$	$Log_{10}(N_0/N_t)$	Reduction (%)	$Log_{10} N_0$	$Log_{10}(N_0/N_t)$	Reduction (%)
0	15	6.52 ± 0.01	2.30 ± 0.08	99.49 ± 0.09	6.18 ± 0.08	0	0
	30		2.43 ± 0.02	99.63 ± 0.02		0	0
	60		2.91 ± 0.01	99.88 ± 0.01		0	0
	180		4.70 ± 0.01	99.998 ± 0.001		2.01 ± 0.35	98.7 ± 0.9
0.05	15	6.67 ± 0.03	0.11 ± 0.06	22.3 ± 10.3	6.59 ± 0.07	0	0
	30		0.21 ± 0.01	37.8 ± 1.8		0.36 ± 0.22	50.3 ± 23.0
	60		0.43 ± 0.09	61.9 ± 7.9		0.63 ± 0.12	76.0 ± 6.3
	180		1.37 ± 0.22	95.1 ± 2.3		1.38 ± 0.24	95.1 ± 2.4
0.10	15	6.67 ± 0.03	0.10 ± 0.05	20.8 ± 9.2	6.59 ± 0.07	0	0
	30		0.18 ± 0.04	33.9 ± 6.1		0.33 ± 0.15	50.0 ± 16.7
	60		0.36 ± 0.07	55.4 ± 6.6		0.46 ± 0.15	63.5 ± 12.0
	180		2.21 ± 0.42	99.1 ± 0.7		1.23 ± 0.06	94.1 ± 0.8

the bactericidal mechanism was determined. The results are addressed in the next section.

3-4) Bactericidal mechanism

3-4-1) Stability of nanorods in water In our previous study,[16] we showed that the bactericidal activity of 10–20 nm-sized particles of $Mg_{1-x}Cu_xO$ in the water suspension depends on the speed at which they dissolve and the nanoparticles of $Mg_{1-x}Cu_x(OH)_2$ precipitate. These results incited us to also probe the dissolution of CuO and $Cu_{0.9}Mg_{0.1}O$ nanorods after 180 min of immersion in water, according to the protocol described in the Experimental section 2.6. The concentrations of the cupric and Mg^{2+} ions released from the CuO and $Cu_{0.9}Mg_{0.1}O$ nanorods in water after 180 min were quantified by AES analyses. The pH of the supernatant was measured at the same specified time used for evaluating bactericidal performances. The concentrations of divalent cations (Mg^{2+} and Cu^{2+}) at 180 min and the pH values at the different immersion times are gathered together in Table 2.

The solubility of CuO in water measured by McDowell *et al.*[15] is 2.9×10^{-5} mol L^{-1} or 1.84 mg L^{-1} at 25 °C. In Table 2, the concentration in cupric ions, released from CuO nanorods after 180 min, is five times lower than this solubility limit. In a conventional dissolution–precipitation mechanism, the surface dissolution of particles releases both hydroxide and Cu^{2+} ions into the supernatant, thus increasing its pH. In Table 2, the pH increase remains very low in magnitude within the first 180 min after the immersion of CuO nanorods in water. This result is consistent with the low concentration of Cu^{2+} detected in the supernatant by AES. No $Cu(OH)_2$ particles can precipitate as long as the supersaturation in cupric and hydroxide ions of the supernatant has not been reached (*i.e.* for concentration higher than 1.84 mg L^{-1} in Cu^{2+}). In parallel, CuO and $Cu_{0.9}Mg_{0.1}O$ nanorods were immersed in water over a long period of 960 min in order to enhance the dissolution and more easily detect any hydroxide by-product thus formed by *ex situ* XRPD and IR spectroscopy analyses. The XRPD pattern and IR spectra of the immersed and raw powders are compared in Fig. 5.

Table 2 Time dependent evolutions of the pH for a suspension of CuO and $Cu_{0.9}Mg_{0.1}O$ nanorods in water (1 mg mL^{-1}). Concentrations in magnesium and copper ions released by the nanorods after 180 min of immersion in water (n.d. = not determined)

	CuO		$Cu_{0.9}Mg_{0.1}O$		
Immersion time (min)	pH	Cu^{2+} (mg L^{-1})	pH	Mg^{2+} (mg L^{-1})	Cu^{2+} (mg L^{-1})
0	5.7	n.d.	6.2	n.d.	n.d.
15	6.07	n.d.	10.1	n.d.	n.d.
30	6.08	n.d.	10.2	n.d.	n.d.
60	6.24	n.d.	10.11	n.d.	n.d.
180	5.86	0.36	10.13	5.87	0.57

After 960 min, no formation of $Cu(OH)_2$ is detected by XRPD, as shown in Fig. 5a. In addition, no stretching vibration bands ν of hydroxyl groups, characteristics of $Cu(OH)_2$,[17] appear in the wavenumber region between 3900 and 2500 cm^{-1} of the IR spectrum collected after 960 min (Fig. 5b). Only a very broad vibration band is observed in this wavenumber region which is attributed to the elongation vibration ν of the O–H bonds within water molecules adsorbed at the surface of the nanorods. Both XRPD and IR analyses clearly demonstrate that a supersaturation in cupric and hydroxide ions of the supernatant has not yet been reached during the 960 min following the immersion of CuO nanorods in water. The dissolution kinetics of these particles is therefore extremely slow despite their small size.

In Table 2, an increase of four pH units takes place in the first 180 min after the immersion of the $Cu_{0.9}Mg_{0.1}O$ nanorods in water. The hydroxide ions released in large amounts from the surface dissolution of nanorods are responsible for such an increase. 10 mol% of magnesium in CuO (*i.e.* $Cu_{0.9}Mg_{0.1}O$) clearly accelerates the dissolution kinetics of nanorods. $Cu_{0.9}Mg_{0.1}O$ nanorods are smaller in size and much less agglomerated to each other than CuO nanorods (Fig. 4) which

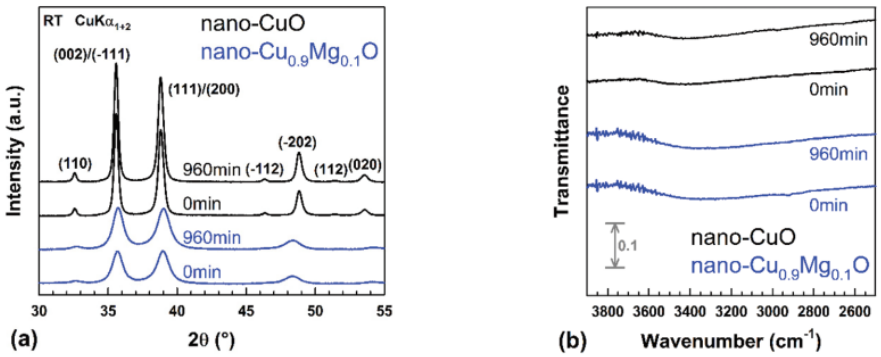

Fig. 5 XRPD patterns (a) and IR transmission spectra (b) collected *ex situ* and at room temperature (RT) on the nanometer-sized particles of CuO and $Cu_{0.9}Mg_{0.1}O$ before and after 960 min of immersion in liquid water.

makes their dissolution faster due to the larger exposed surface to water molecules. In water, the different crystallized domains existing within each nanorod (see Discussion in sections 3.1 and 3.2) can separate from each other and thus also accelerate the dissolution of nanorods. After 180 min following the immersion of $Cu_{0.9}Mg_{0.1}O$ nanorods in water, the mass concentration in Mg^{2+} ions released in the supernatant (5.87 mg L^{-1} in Table 2) is below the solubility limit of $Mg(OH)_2$ in water (6.53 mg L^{-1} in ref. 33). Despite the basic pH (Table 2), no $Mg(OH)_2$ particles will precipitate until supersaturation in Mg^{2+} ions of the supernatant is reached. Even after 960 min, the diffraction peak at $2\theta \approx 38°$ and the stretching vibration band ν_{OH} at 3700 cm^{-1} characteristic of $Mg(OH)_2$ [34] are still not visible in the XRPD pattern (Fig. 5a) and the IR spectrum (Fig. 5b), respectively. Wetteland *et al.*[35] showed that the viability of *E. coli* is in no way affected by any increase in the concentration of solvated Mg^{2+} ions up to 5×10^{-2} mol L^{-1} (*i.e.* 1215 mg L^{-1}). Given the very low concentration measured in the supernatant after 180 minutes (Table 2), the released Mg^{2+} ions have therefore no bactericidal effect on *E. coli* and very likely on *S. aureus* as well.

In the supernatant, the mass concentration of Cu^{2+} ions released from $Cu_{0.9}Mg_{0.1}O$ is surprisingly 10 times lower than that of Mg^{2+} ions (Table 2). By considering that the initial Cu/Mg molar ratio of 9/1 is preserved in the course of the surface dissolution of $Cu_{0.9}Mg_{0.1}O$ nanorods, the total amount of cupric ions released after 180 min should have been 137.43 mg L^{-1} given the magnesium concentration measured by AES (Table 2). As only 0.57 mg L^{-1} of these Cu^{2+} ions remains in the solution (Table 2), 99.6 wt% of the cupric ions released from $Cu_{0.9}Mg_{0.1}O$ nanorods must have precipitated as CuO or $Cu(OH)_2$ due to the basic pH of the supernatant. This conclusion is consistent with the low solubility in water of CuO[15] (*i.e.* 1.84 mg L^{-1}) or $Cu(OH)_2$ [36] (*i.e.* 11.2 μg L^{-1}). Even after 960 min, no trace of $Cu(OH)_2$ was detected by XRPD (Fig. 5a) and by IR spectroscopy (Fig. 5b). Therefore, freshly precipitated CuO nanoparticles necessarily coexist with undissolved $Cu_{0.9}Mg_{0.1}O$ nanorods in the suspension. As both oxides have the same crystal structure, the presence of CuO is impossible to detect in the XRPD pattern collected after 960 min (Fig. 5a) due to the overlap of its broad diffraction peaks with those of $Cu_{0.9}Mg_{0.1}O$. We conclude that after 180 min of immersion of $Cu_{0.9}Mg_{0.1}O$ nanorods at 1 mg mL^{-1}, the initial Cu loading of 755 mg L^{-1} is distributed as follows: 0.57 mg L^{-1} in the supernatant, 137.43 mg L^{-1} in freshly precipitated CuO nanoparticles and the rest (617 mg L^{-1}) in undissolved $Cu_{0.9}Mg_{0.1}O$ nanorods. The significant increase of lethal activity measured for the $Cu_{0.9}Mg_{0.1}O$ sample between 60 and 180 min (*e.g.* from ≈0.4 Log_{10} to ≈2.2 Log_{10} for *E. coli* in Table 1) certainly results from the precipitation of these highly active CuO nanoparticles. As magnesium seems to accelerate the dissolution of $Cu_{1-x}Mg_xO$ nanorods, the higher the magnesium content x, the faster they will dissolve and the more CuO particles will be precipitated. After 180 min, the difference in bactericidal activity between $Cu_{0.95}Mg_{0.05}O$ and $Cu_{0.9}Mg_{0.1}O$ is higher for *E. coli* (1.4 to 2.2 Log_{10} in Table 1) than for *S. aureus* (1.2 to 1.4 Log_{10} in Table 1). This reflects the impact of the amount of CuO nanoparticles precipitated on the bactericidal activity of $Cu_{1-x}Mg_xO$ nanorods because CuO is much more active against *E. coli* (4.7 Log_{10} in Table 1) than against *S. aureus* (2 Log_{10} in Table 1).

3-4-2) Production of free oxygen radicals Hydrogen peroxide is a by-product of the normal metabolism of oxygen in aerobic living organisms.[37] H_2O_2 is present at millimolar concentrations in the culture supernatant of *E. coli* and *S. aureus*[38] despite their catalase activity. It is well known that solvated cupric ions can catalyse the generation of ROS from aqueous H_2O_2 through a Fenton-like redox cycling between Cu^{2+} and Cu^+/Cu^{3+} ions[13,14] (eqn (1)–(5)).

$$Cu^{2+} + H_2O_2 \rightarrow Cu^+ + O_2^{\bullet -} + 2H^+ \quad (1)$$

$$Cu^+ + H_2O_2 \rightarrow Cu^{2+} + OH^- + HO^\bullet \quad (2)$$

$$Cu^+ + H_2O_2 \rightarrow Cu^{3+} + 2OH^- \quad (3)$$

$$Cu^{3+} + H_2O_2 \rightarrow Cu^{2+} + O_2^{\bullet -} + 2H^+ \quad (4)$$

$$Cu^{2+} + O_2^{\bullet -} \rightarrow Cu^+ + O_2 \quad (5)$$

Cupric ions on the surface of nanoparticles can also catalyse the generation of free $O_2^{\bullet -}/HO_2^\bullet$ and $HO^\bullet$ radicals (heterogeneous catalysis) as solvated Cu^{2+} ions do in solution (homogeneous catalysis). The minimal inhibitory concentrations (MIC) in free cupric ions for the growth of *E. coli* and *S. aureus* are 25 mg L^{-1} and 12.5 mg L^{-1}, respectively.[12] To produce lethal amounts of radicals, the concentration of free cupric ions must be equal to or greater than the MIC (minimal bactericidal concentration MBC ≥ MIC). Given the very low concentrations measured in the supernatant after 180 min (Table 2), the solvated Cu^{2+} released from CuO and $Cu_{0.9}Mg_{0.1}O$ cannot have a bactericidal effect on *E. coli* and *S. aureus*.

The bactericidal activity in water of CuO and the magnesium counterparts can therefore only come from the radicals produced by nanorods themselves. Applerot *et al.*[4] have shown that superoxide $O_2^{\bullet -}/HO_2^\bullet$ radicals are produced by a suspension of CuO nanoparticles. We suspect that the Mg substitution in CuO reduces the amount of these free radicals generated, thus causing a large decrease of its bactericidal kinetics against *E. coli* in particular. Then, electron paramagnetic resonance (EPR) spin trapping experiments were performed to estimate and compare the amount of the free oxygen radicals produced by CuO and $Cu_{0.9}Mg_{0.1}O$ nanorods in the presence of H_2O_2. In Fig. 6a, aqueous suspensions of CuO and $Cu_{0.9}Mg_{0.1}O$ nanorods containing H_2O_2 and DMPO exhibit very similar EPR spectra. Each experimental EPR spectrum can be satisfactorily fitted with only two superimposed signals characterized by the spin-Hamiltonian parameters typical of two DMPO-adducts of oxygen-centered radicals, namely $^\bullet$DMPO-O_2^-/O_2H (12-line signal; a_N = 1.427 ± 0.017 mT, a_H^β = 1.141 ± 0.011 mT, a_H^γ = 0.140 ± 0.010 mT, g = 2.0058) and $^\bullet$DMPO-OH (4-line signal; a_N = 1.507 ± 0.004 mT, a_H^β = 1.477 ± 0.007 mT, g = 2.0057)[39,40] (Fig. 6a). Whatever the water suspen-

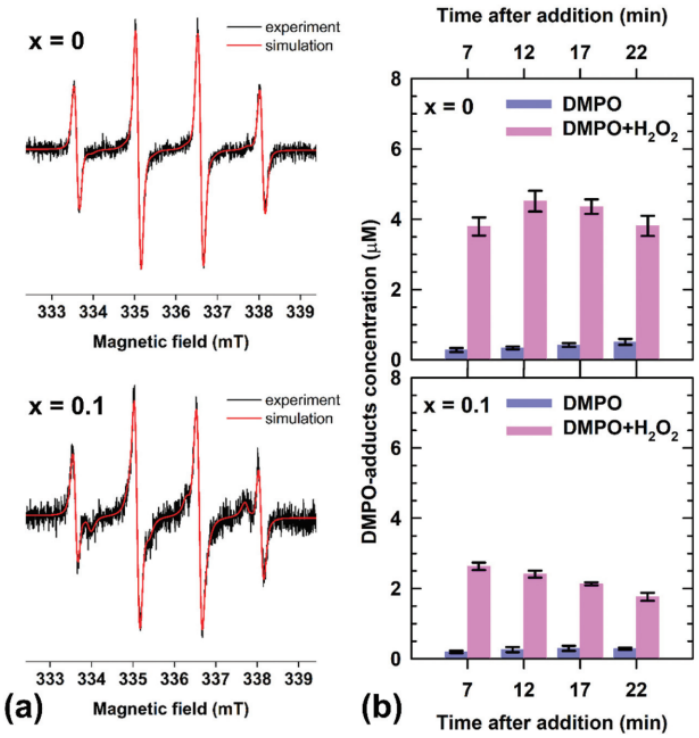

Fig. 6 (a) Normalized experimental (black line) and simulated (red line) EPR spectra measured 7 min after the addition of hydrogen peroxide ($c_0(H_2O_2)$ = 0.03 M) to the aerated water suspensions of CuO (x = 0) and $Cu_{0.9}Mg_{0.1}O$ (x = 0.1) nanorods (loading 1 mg mL^{-1}) in the presence of the DMPO spin trapping agent (c_0(DMPO) = 0.04 M). The relative concentration of $^{\bullet}$DMPO-OH and $^{\bullet}$DMPO-O_2^-/O_2H spin adducts evaluated from the simulated spectra are as follows: CuO (86.7% and 13.3%) and $Cu_{0.9}Mg_{0.1}O$ (59.2% and 40.8%). (b) Time evolutions of the total concentration of DMPO-adducts monitored at 20 °C with or without the addition of H_2O_2 to the aerated water suspensions of the studied nanorods in the presence of DMPO.

sion of nanorods, the relative concentration of the $^{\bullet}$DMPO-OH spin adducts deduced from these fits is higher than that of the $^{\bullet}$DMPO-O_2^-/O_2H ones (ratios ≈9 : 1 and ≈6 : 4 for CuO and $Cu_{0.9}Mg_{0.1}O$, respectively). Finkelstein *et al.*[41] evaluated that approximately 3% of the $^{\bullet}$DMPO-O_2H adducts formed during a spin-trapping experiment can directly decompose into the $^{\bullet}$DMPO-OH adducts. Given the ≈9 : 1 ratio of adducts for CuO, the partial dismutation of the $^{\bullet}$DMPO-O_2H adducts could only slightly increase the relative proportion of the $^{\bullet}$DMPO-OH adducts detected in the water suspension. Thereby, the $^{\bullet}$DMPO-OH adducts result mainly from the trapping of free hydroxyl radicals intrinsically generated by CuO nanorods in the water suspension. On the other hand, the partial dismutation of the $^{\bullet}$DMPO-O_2H adducts could have a greater contribution to the relative proportion of the $^{\bullet}$DMPO-OH adducts for $Cu_{0.9}Mg_{0.1}O$ nanorods than for CuO because the ratio of adducts is this time only ≈6 : 4 for the former.

The same EPR spin trapping experiments were also performed without adding H_2O_2 to the medium to determine its role in radical production. The fitting of these EPR spectra is presented in section S3 of the ESI.† The time evolutions of the total concentration of DMPO spin adducts produced by nanoparticles in the presence and absence of H_2O_2 are compared in Fig. 6b. In the absence of H_2O_2, the total concentration of DMPO-adducts monitored in both aerated water suspensions of CuO and $Cu_{0.9}Mg_{0.1}O$ nanorods is less than 0.5 μmol L^{-1} within the first 22 min after adding DMPO. The similar amount of radicals produced by CuO and $Cu_{0.9}Mg_{0.1}O$ cannot explain why their activities are so different. The addition of H_2O_2 to water suspensions of both CuO and $Cu_{0.9}Mg_{0.1}O$ nanorods greatly increases the total concentration of DMPO-adducts formed within the first 7 min. However, $Cu_{0.9}Mg_{0.1}O$ produces 1.4 times less free oxygen radicals than CuO during this period which is consistent with the low activity of the former. Hydrogen peroxide therefore plays a key role in the bactericidal mechanism of those oxides. In the next 15 min, the total concentration of DMPO-adducts produced by $Cu_{0.9}Mg_{0.1}O$ nanorods gradually decreases while it remains around 4 μmol L^{-1} on average for CuO nanorods (Fig. 6b). In Table 2, the pH of the supernatant sharply increases from ≈6 to ≈10 in the first 15 min after the immersion of $Cu_{0.9}Mg_{0.1}O$ nanorods in water whereas pH remains around 6 for CuO

nanorods. It is well known that alkaline media[42–45] can promote the decomposition of hydrogen peroxide into free oxygen radicals, *i.e.* $O_2^{\bullet-}/HO_2^{\bullet}$ and $HO^{\bullet}$. However, for the $O_2^{\bullet-}/HO_2^{\bullet}$ trapping by DMPO, both the rate constant and the stability of spin-adducts decrease significantly with increasing pH.[46,47] The small total concentration of DMPO-adducts in the suspension of $Cu_{0.9}Mg_{0.1}O$ nanorods as well as its slow decay over time are attributed to the decomposition of these adducts at the alkaline pH imposed by the partial dissolution of these nanorods in water (Table 2).

Hydroxyl radical is the most active among all ROS because it can initiate a free radical chain reaction leading to extensive lipid and organic peroxide formation in aerobic living organisms (oxidative stress).[48] The above EPR spin trapping study reveals that, the toxicity of the CuO nanoparticles is mainly due to hydroxyl radicals $HO^{\bullet}$ produced in the presence of H_2O_2, in contrast to what Applerot *et al.*[4] claimed. This discrepancy may result from the saline solution used (instead of sterile water in our study) as a medium for antibacterial assays in this latter study.[4] Indeed, chloride anions of the saline solution can affect the toxicity of particles because they can increase the concentration of Cu^{2+} ions released from particles. In such a situation, free oxygen radicals can be produced by both particles and solvated cupric ions, leading to a different $HO^{\bullet}/O_2^{\bullet-}$ ratio than ours. As an example, Li *et al.* showed that the medium components affect the toxicity of ZnO particles.[49] The lower bactericidal performance of magnesium-substituted CuO particles results from the reduction in both the total amount of oxygen radicals produced and the $HO^{\bullet}/O_2^{\bullet-}$ ratio. Why? At the surface of nanorods, the high proportion of incomplete coordination spheres at the divalent cationic sites naturally promote the adsorption of hydrogen peroxide molecules, the initial step allowing the formation of free oxygen radicals. However, between two cations, Cu^{2+} ions are the most active because they have a greater ability to be sub-coordinated to ligands (*i.e.* four- or five-fold coordinated) than Mg^{2+} ones and they can catalyse the generation of free oxygen radicals from aqueous H_2O_2 through a Fenton-like redox cycling between Cu^{2+} and Cu^{+}/Cu^{3+} ions. Thereby, we believe that the decrease in free oxygen radicals amount produced when partially substituted Cu^{2+} by Mg^{2+} in CuO nanorods arises from the decrease in the number of sub-coordinated Cu^{2+} ions available for H_2O_2 adsorption at the surface. In Table 1, the reduction in the viability after 180 min of contact with CuO nanorods is only around 2 Log_{10} for *S. aureus* while it was as high as 4.7 Log_{10} for *E. coli*. It has been shown that carotenoid pigments such as staphyloxanthin, giving the golden color to the *S. aureus* bacterial envelope, have antioxidant properties[50] leading to H_2O_2 resistance.[51] Conversely, *E. coli* are deprived of this antioxidant pigment. These pigments can help *S. aureus* to detoxify hydroxyl radicals produced by CuO nanorods adsorbed onto their envelopes, thus making them less sensitive to treatment than *E. coli*. However, the absence of any activity against *S. aureus* for contact times shorter than 60 min would rather result from a very weak adsorption of CuO nanorods on their envelopes; the small number of hydroxyl radicals generated by these few adsorbed particles are then easily detoxified by the bacteria.

4-Conclusion and perspective

In this study, the simple thermal decomposition of the single source precursor $Cu_{1-x}Mg_x(OH)_2$, prepared in advance by co-precipitation, leads to well crystallized $Cu_{1-x}Mg_xO$ nanorods of 50–60 nm length. By studying different $Cu_{1-x}Mg_xO$ compositions, we demonstrate that rigorous microstructural analyses of the powder XRD data allowed us to achieve sufficient precision on lattice parameters to determine content x in magnesium above which the Vegard's law or the solubility is not verified anymore in these nanoscale oxides. The extent of this new $Cu_{1-x}Mg_xO$ solid solution is limited to $x = 0.1$ due to the incapacity of the distorted NaCl-type structure of CuO to accommodate more than 10% of regular coordination $[MgO_6]$ octahedra. To confirm what our microstructural analyses have revealed, neutron diffraction was used to detect the small amount of MgO nanoparticles present as an impurity in a 10 g sample beyond this solubility limit. In this series, CuO nanorods remain the most active against *E. coli* and *S. aureus* with reductions in the viability of 99.998% and 98.7% after only 180 min in water, respectively. The dissolution kinetics of the CuO particles is extremely slow in water despite their nanoscale size. The partial substitution of cupric ions in CuO by Mg^{2+}, even if it does not exceed 10 mol%, increases by a factor of 40 the dissolution of the nanorods after 180 min in water (0.045 wt% and 1.8 wt% for CuO and $Cu_{0.9}Mg_{0.1}O$, respectively). Although Mg substitution increases the solubility of CuO nanoparticles in water, the pH increase induced by the dissolution causes the re-precipitation of ≈99.6 wt% of the released cupric ions in the form of pure CuO particles. For pure and magnesium substituted CuO, the released cupric ions have no bactericidal effect because the concentration after 180 min is much lower than the MIC. These CuO nanorods kill bacteria in water because they produce a large quantity of free oxygen radicals in the presence of H_2O_2 only, the majority of which are highly toxic hydroxyl radicals $HO^{\bullet}$. Mg^{2+} has a detrimental effect on this production, thus explaining the lowest bactericidal performances of $Cu_{1-x}Mg_xO$ nanorods.

Despite an almost similar content of the substituted cations (*i.e.* Mg^{2+} and Zn^{2+}), the bactericidal activities of $Cu_{0.9}Mg_{0.1}O$ and $Cu_{0.88}Zn_{0.12}O$ [11] (unless this sample is biphasic) significantly differ, thus pointing out a synergistic effect of Cu^{2+} with Zn^{2+} that does not exist with Mg^{2+}. These cationic substitutions in the semiconducting CuO oxide, even if they are both isovalent, can differentially modify the reactivity of the nanoparticle surface towards the adsorption of H_2O_2 molecules and their dissociation into hydroxyl radicals. The high bactericidal activity of $Cu_{1-x}Zn_xO$ particles could be related to the large number of active sites available for H_2O_2 adsorption/dissociation because of the ability of both cations to be sub-coordinated to oxide anions. This point deserves to be studied in detail in the future by modelling the adsorption and dis-

sociation of H_2O_2 molecules on the surface of $Cu_{1-x}Zn_xO$ and $Cu_{1-x}Mg_xO$ by density functional theory (DFT) calculations.

Cupric oxide is a compound of interest especially in the context of the past and current global health crises. Cupron Scientific Company[52] demonstrates that the impregnation of respiratory protective face masks with 2.2 wt% of micron-sized particles of CuO is able to reduce the transmission of human influenza A virus (H1N1) and avian influenza virus (H9N2) without altering their filtration capacities. Recently, Hosseini *et al.*[53] revealed that the infectivity from SARS-CoV-2 can be reduced by 99.9% on average after the first hour of contact with a CuO film. These authors conclude that the leachate from the CuO film did not significantly inactivate the virus, even over 24 h of exposure (the virus was never in contact with the solid in this experiment). Thereby, Hosseini *et al.*[53] demonstrated that inactivation of viruses requires physical contact with CuO particles. We therefore believe that the highly toxic hydroxyl radicals $HO^{\bullet}$ produced by CuO nanoparticles play a key role in the inactivation of SARS-CoV-2. A precise knowledge of the toxicity of CuO nanoparticles towards bacteria and, at the same time, towards viruses is now available.

Author contributions

Batiste Clavier: investigation, formal analysis, and visualization. Antonii Zhadan: investigation. Téo Baptiste: investigation. Fabien Boucher: investigation (Atomic Emission Spectroscopy). Amandine Guiet: investigation (Transmission Electron Microscopy). Florence Porcher: investigation (Neutron Diffraction). Vlasta Brezová: methodology, investigation, and data curation (Electron Paramagnetic Resonance). Christine Roques: methodology, investigation, and data curation (Bactericidal activity). Gwenaël Corbel: conceptualization, methodology, validation, formal analysis, data curation, writing – original draft, writing – review & editing, visualization, supervision, project administration, and funding acquisition.

Conflicts of interest

There are no conflicts of interest to declare.

Acknowledgements

The French Ministry of Higher Education, Research and Innovation and Le Mans University are acknowledged for providing a doctoral grant to BC. Laboratoire Léon Brillouin is thanked for beam time allocation on the G4.4 diffractometer. The EPR study was financially supported by the Scientific Grant Agency of the Ministry of Education, Science, Research and Sport of the Slovak Republic (VEGA Project 1/0064/21). VB thanks the Ministry of Education, Science, Research and Sport of the Slovak Republic for funding within the scheme "Excellent research teams". CR thanks the Fonderephar for its technical support.

References

1 Santé Publique France, *Enquête nationale de prévalence des infections nosocomiales et des traitements anti-infectieux en établissements de santé, mai-juin 2017* (**https://www.santepubliquefrance.fr/maladies-et-traumatismes/infections-associees-aux-soins-et-resistance-aux-antibiotiques/infections-associees-aux-soins/documents/enquetes-etudes/enquete-nationale-de-prevalence-des-infections-nosocomiales-et-des-traitements-anti-infectieux-en-etablissements-de-sante-mai-juin-2017**), 2019, pp. 1–270.
2 N. Thakur, Anu, K. Kumar and A. Kumar, *Dalton Trans.*, 2021, **50**, 6188–6203.
3 A. Azam, A. S. Ahmed, M. Oves, M. S. Khan and A. Memic, *Int. J. Nanomed.*, 2012, **7**, 3527–3535.
4 G. Applerot, J. Lellouche, A. Lipovsky, Y. Nitzan, R. Lubart, A. Gedanken and E. Banin, *Small*, 2012, **8**, 3326–3337.
5 M. Hans, A. Erbe, S. Mathews, Y. Chen, M. Solioz and F. Mücklich, *Langmuir*, 2013, **29**, 16160–16166.
6 C. Gunawan, W. Y. Teoh, C. P. Marquis and R. Amal, *ACS Nano*, 2011, **5**, 7214–7225.
7 O. Menkissoglu and S. E. Lindow, *Phytopathology*, 1991, **81**, 1258–1263.
8 S. U. Din, M. Sajid, M. Imran, J. Iqbal, B. A. Shah, M. Azeem ullah and S. Shah, *Mater. Res. Express*, 2019, **6**, 085022.
9 Y. Lv, L. Li, P. Yin and T. Lei, *Dalton Trans.*, 2020, **49**, 4699–4709.
10 L. Vegard, *Z. Phys.*, 1921, **5**, 17–26.
11 E. Malka, I. Perelshtein, A. Lipovsky, Y. Shalom, L. Naparstek, N. Perkas, T. Patick, R. Lubart, Y. Nitzan, E. Banin and A. Gedanken, *Small*, 2013, **9**, 4069–4076.
12 Z. H. Zhao, Y. Sakagami and T. Osaka, *Bull. Chem. Soc. Jpn.*, 1998, **71**, 939–945.
13 A. N. Pham, G. Xing, C. J. Miller and T. D. Waite, *J. Catal.*, 2013, **301**, 54–64.
14 T. T. M. Nguyen, H.-J. Park, J. Y. Kim, H.-E. Kim, H. Lee, J. Yoon and C. Lee, *Environ. Sci. Technol.*, 2013, **47**, 13661–13667.
15 L. A. McDowell and H. L. Johnston, *J. Am. Chem. Soc.*, 1936, **58**, 2009–2014.
16 B. Clavier, T. Baptiste, Z. Barbieriková, T. Hajdu, A. Guiet, F. Boucher, V. Brezová, C. Roques and G. Corbel, *Mater. Sci. Eng., C*, 2021, **123**, 111997.
17 B. Clavier, T. Baptiste, A. Zhadan, A. Guiet, F. Boucher, V. Brezová, C. Roques and G. Corbel, *J. Mater. Chem. B*, 2022, **10**, 779–794.
18 J. I. Langford, *J. Appl. Crystallogr.*, 1978, **11**, 10–14.
19 T. H. de Keijser, J. I. Langford, E. J. Mittemeijer and A. B. P. Vogels, *J. Appl. Crystallogr.*, 1982, **15**, 308–314.
20 J. I. Langford, D. Louër, E. J. Sonneveld and J. W. Visser, *Powder Diffr.*, 1986, **1**, 211–221.
21 J. I. Langford, International Conference "Accuracy in Powder Diffraction II", May 26-29, 1992 at NIST, Gaithersburg, MD, USA, 1992, 110–126.

22 G. Courbion and G. Ferey, *J. Solid State Chem.*, 1988, **76**, 426–431.
23 A. Le Bail, H. Duroy and J. L. Fourquet, *Mater. Res. Bull.*, 1988, **23**, 447–452.
24 J. Rodriguez Carvajal, *Phys. B*, 1993, **192**, 55–69.
25 P. Thompson, D. E. Cox and J. B. Hastings, *J. Appl. Crystallogr.*, 1987, **20**, 79–83.
26 R. Delhez, T. H. de Keijser and E. J. Mittemeijer, *Fresenius' Z. Anal. Chem.*, 1982, **312**, 1–16.
27 S. Brunauer, P. H. Emmett and E. Teller, *J. Am. Chem. Soc.*, 1938, **60**, 309–319.
28 S. Stoll and A. Schweiger, *J. Magn. Reson.*, 2006, **178**, 42–55.
29 H. M. Rietveld, *Acta Crystallogr.*, 1967, **22**, 151–152.
30 S. Asbrink and L.-J. Norrby, *Acta Crystallogr., Sect. B: Struct. Crystallogr. Cryst. Chem.*, 1970, **26**, 8–15.
31 N. V. P. Chaudhary, J. K. Murthy and A. Venimadhav, *Solid State Commun.*, 2016, **247**, 36–39.
32 R. D. Shannon, *Acta Crystallogr., Sect. A: Cryst. Phys., Diffr., Theor. Gen. Crystallogr.*, 1976, **32**, 751–767.
33 *CRC Handbook of Chemistry and Physics 2008–2009: A Ready-Reference Book of Chemical and Physical Data*, ed. D. R. Lide, CRC Press, Boca Raton, Florida, USA, 2008.
34 B. Clavier, T. Baptiste, F. Massuyeau, A. Jouanneaux, A. Guiet, F. Boucher, V. Fernandez, C. Roques and G. Corbel, *J. Mater. Chem. B*, 2020, **8**, 100–113.
35 C. L. Wetteland, N.-Y. T. Nguyen and H. Liu, *Acta Biomater.*, 2016, **35**, 341–356.
36 *Handbook of Inorganic Chemicals*, ed. P. Patnaik, McGraw-Hill, 2003.
37 W. Dröge, *Physiol. Rev.*, 2002, **82**, 47–95.
38 C. D. Pericone, K. Overweg, P. W. M. Hermans and J. N. Weiser, *Infect. Immun.*, 2000, **68**, 3990.
39 M. Hricovíni, M. Mazúr, A. Sîrbu, O. Palamarciuc, V. B. Arion and V. Brezová, *Molecules*, 2018, **23**, 17.
40 D. Dvoranová, Z. Barbieriková, M. Mazúr, E. I. García-López, G. Marcì, K. Lušpai and V. Brezová, *J. Photochem. Photobiol., A*, 2019, **375**, 100–113.
41 E. Finkelstein, G. M. Rosen and E. J. Rauckman, *Mol. Pharmacol.*, 1982, **21**, 262.
42 Z. M. Galbács and L. J. Csányi, *J. Chem. Soc., Dalton Trans.*, 1983, **11**, 2353–2357.
43 L. J. Csányi, L. Nagy, Z. M. Galbács and I. Horváth, *Z. Phys. Chem.*, 1983, **138**, 107–116.
44 D. Dong and G. F. Vandegrift, *Nucl. Sci. Eng.*, 1997, **126**, 213–223.
45 C. M. Miller and R. L. Valentine, *Water Res.*, 1999, **33**, 2805–2816.
46 E. Finkelstein, G. M. Rosen and E. J. Rauckman, *J. Am. Chem. Soc.*, 1980, **102**, 4994–4999.
47 A. Allouch, R. P. Lauricella and B. N. Tuccio, *Mol. Phys.*, 2007, **105**, 2017–2024.
48 B. Chance, H. Sies and A. Boveris, *Physiol. Rev.*, 1979, **59**, 527–605.
49 M. Li, L. Zhu and D. Lin, *Environ. Sci. Technol.*, 2011, **45**, 1977–1983.
50 G. Y. Liu, A. Essex, J. T. Buchanan, V. Datta, H. M. Hoffman, J. F. Bastian, J. Fierer and V. Nizet, *J. Exp. Med.*, 2005, **202**, 209–215.
51 V. Antonic, A. Stojadinovic, B. Zhang, M. J. Izadjoo and M. Alavi, *Infect. Drug Resist.*, 2013, **6**, 175–186.
52 G. Borkow, S. S. Zhou, T. Page and J. Gabbay, *PLoS One*, 2010, **5**, e11295.
53 M. Hosseini, A. W. H. Chin, S. Behzadinasab, L. L. M. Poon and W. A. Ducker, *ACS Appl. Mater. Interfaces*, 2021, **13**, 5919–5928.